

Exploring Quantumness at Long-Baseline Neutrino Experiments

Murshed Alam  ^a, **Vedran Brdar**  ^a and **Dibya S. Chattopadhyay**  ^a

^a*Department of Physics, Oklahoma State University, Stillwater, OK 74078, USA*

E-mail: murshed.alam@okstate.edu, vedran.brdar@okstate.edu,
dibya.chattopadhyay@okstate.edu

ABSTRACT: Violations of classicality can be probed through measurements performed on a system at different times, as proposed by Leggett and Garg. Specifically, violations of Leggett-Garg inequalities suggest the presence of quantum effects in macroscopic systems. Long-baseline neutrino experiments provide some of the longest available propagation distances over which such tests can be performed. Previous studies of Leggett-Garg tests in the neutrino sector have largely focused on showing that the oscillation probabilities can violate classical bounds for certain parameter choices. In this work, we develop a more complete and data-driven framework that treats both the distributions representing the classical and quantum behavior, as well as the experimental uncertainties. We consider MINOS, T2K, NOvA, as well as the upcoming DUNE, and present the respective statistical significance for distinguishing quantum behavior from classical scenarios at these long-baseline neutrino experiments. Among them, we find that T2K yields the most significant violation of classicality, at the level of $\sim 14\sigma$, with NOvA and projections for DUNE also resulting in a significance of more than 5σ .

Contents

1	Introduction	1
2	Theory	3
2.1	Application at Neutrino Oscillation Experiments	4
2.2	Generalized Leggett-Garg Strings	4
2.2.1	Explicit Leggett-Garg Strings for the Quantum and Classical Cases	5
2.2.2	Leggett-Garg Strings in terms of Neutrino Survival Probabilities	6
2.2.3	Comparing K_3^{Q++} and K_3^{\max}	7
2.3	The RMS z -score	8
2.3.1	Defining the z -score	8
2.3.2	Defining the RMS z -score	10
3	Implementation	11
3.1	Obtaining the Energy Triplets for the Leggett-Garg Strings	11
3.2	Sampling in the Presence of Asymmetric Probability Uncertainties	13
4	Results	14
4.1	Fraction of Triplets that Violate the Leggett-Garg Inequality	16
4.2	RMS z -score	18
4.3	Quantifying the Distributions	20
4.3.1	Fitting the Data with Gaussian PDFs	20
4.3.2	Fitting the Data with Gaussian CDFs	20
4.4	Comparing the Significance of Quantumness Across Experiments	22
4.5	DUNE Results with Varying Systematic Error	24
4.6	Summary of the Results	25
5	Conclusions	25

1 Introduction

Quantum mechanics has been established for about a century and today stands at the forefront of modern research. Its principles govern phenomena describing structure of matter and the behavior of elementary particles, which is far beyond the realm of classical mechanics. It is, however, nontrivial to set up a test to determine whether a system behaves in a classical or a quantum way. Among the most studied examples for that are Bell's inequalities [1], which quantify the correlations between measurements on spatially separated systems and provide a way to test whether these correlations require quantum mechanics for their explanation [2, 3].

Another probe of quantumness, which can be applied to a single system that is measured at different times, was formulated by Leggett and Garg [4, 5]. It attempts to test two fundamental classical criteria: macroscopic realism [4–7] and non-invasive measurability [5, 8, 8–12]. The former suggests that measurements reveal pre-existing values, while the latter asserts that measurements can be made without altering the state of the system. Correlations between measurements on a system at different times are bounded in a purely classical scenario, which is quantified by the Leggett–Garg inequality (LGI). Violations of this inequality therefore suggest that the system in question possesses quantum mechanical properties.

Long-baseline neutrino experiments provide some of the longest length scales over which tests of quantumness can be performed. It was pioneered in Ref. [13] that the LGI can be tested in such experiments. In that work, an additional assumption, called stationarity, was made: correlations between measurements are assumed to depend on the durations of the intervals rather than on the absolute times at which the measurements are performed. The authors employed data from the MINOS experiment [14, 15] and found that the LGI is violated at more than 6σ . This claim was recently challenged in Ref. [16], where the authors used modified classical predictions and concluded that LGI violations at MINOS can be quantified only at the $\sim 3\sigma$ level. Since the jury is still out on this, in the present work, we obtain results using approaches from both Refs. [13, 16]. Our main improvement over both, however, lies in the treatment of the width of the experimental energy bins, which are important for creating data sequences used in testing LGI violations. We also introduce a sampling method that handles asymmetric uncertainties on the neutrino survival probability data, and an effective cumulative distribution function (CDF)-based Gaussian fit that is employed for scenarios where a non-Gaussian shape of the classical predictions arise. On the theory side, we treat the two classical prediction schemes [13, 16] and introduce a modified RMS (root-mean-squared) z -score measure for quantifying the degree of non-classicality; our modified RMS z -score definition allows us to probe both the effects of the fraction of data points that violates the LGI, as well as the magnitude of the LGI violation.

In addition to MINOS, we also, for the first time, present results for two leading long-baseline experiments, T2K [17] and NOvA [18], as well as projections for the upcoming DUNE experiment [19, 20]. While it has been shown for several neutrino experiments that one would expect a violation of the classical limit in a certain parameter range [21–25], detailed statistical analysis yielding the significance of LGI violation has only been presented in a few works, including the above Refs. [13, 16] for MINOS and Refs. [26, 27], which featured studies of the Daya Bay [28] and KamLAND [29] reactor antineutrino experiments. In this work, we address this gap by performing a detailed study of present and near-future accelerator-based long-baseline neutrino experiments in the context of LGI violation and ranking these experiments according to their potential for testing it.

The paper is organized as follows. In section 2, we introduce the formalism behind Leggett–Garg (LG) strings and discuss how LGI violations can be tested in neutrino oscillation experiments, focusing on a treatment of both the quantum and classical predictions. Further, we also introduce a modified RMS z -score definition and discuss why it is a well-

suited measure for quantifying quantumness at neutrino experiments. In section 3, we detail our analysis, with discussions on the effects of the width of the experimental energy bins and asymmetric uncertainties often present in neutrino survival probability data. Our findings for all the considered long-baseline experiments are presented in section 4. Finally, we conclude in section 5.

2 Theory

Consider a dichotomic observable \hat{Q} , whose measurement outputs at any time t_i are restricted to ± 1 . The correlation function associated with measurements at times t_i and t_j is defined as

$$C_{ij} \equiv \langle \hat{Q}(t_i) \hat{Q}(t_j) \rangle, \quad (2.1)$$

where $\langle \dots \rangle$ denotes the expectation value, typically evaluated over many realizations of the experiment [5, 8].

Using these correlation functions, the LG parameter, K_n , for measurements at n distinct times is defined as

$$K_n = \sum_{i=1}^{n-1} C_{i(i+1)} - C_{n1}, \quad (2.2)$$

with the simplest LG measure defined as $K_3 = C_{12} + C_{23} - C_{31}$. Classically, the measure K_n is bound as [4, 5]

$$K_n \leq n - 2, \quad (2.3)$$

for $n \geq 3$. This is known as the Leggett-Garg Inequality (LGI).

In neutrino oscillation experiments, a violation of the LGI can arise either from the intrinsic quantum nature of flavor oscillations or from statistical and systematic uncertainties in realistic measurements. It is therefore necessary to consider the corresponding classical LG measure. In several previous studies [13, 26], the classical LG measure has been defined as

$$K_n^C \equiv \sum_{i=1}^{n-1} C_{i(i+1)} - \prod_{i=1}^{n-1} C_{i(i+1)}. \quad (2.4)$$

This is because, for a time-reversal symmetric two-level classical system, the correlation function C_{n1} can be expressed as

$$C_{n1} = \prod_{i=1}^{n-1} C_{i(i+1)}. \quad (2.5)$$

The simplest LG measure (for $n = 3$) takes the form $K_3^C = 1 - (1 - C_{12})(1 - C_{23})$. For $0 \leq C_{12}, C_{23} \leq 1$, it can be shown that K_3^C always satisfies the Leggett-Garg inequality $K_3 \leq 1$. This result can be generalized for K_n^C , and thus, classically, no violations of the LGI should be observed. However, for neutrino experiments, the large statistical and systematic uncertainties on the neutrino oscillation probability can lead to values of the correlation function below zero or above 1, which would lead to violations of the LGI.

We also note that a different technique to model the classical behavior was explored in Ref. [16], and we will discuss this in more detail in section 2.2.1. Our analysis also involves comparing the quantum distribution against such classical predictions.

2.1 Application at Neutrino Oscillation Experiments

In long-baseline neutrino experiments, performing measurements at multiple time intervals is impractical, as the neutrino detection location is fixed. However, special relativity allows us to circumnavigate this issue, as a particle of mass m evolving for a proper time $\Delta\tau$ is associated, in the lab frame, to an interval $\Delta t = (\Delta\tau/m)E$, where E is its energy. Thus, the evolution of the system depends only on the ratio $\Delta t/E$, and varying the neutrino energy at a fixed baseline effectively emulates measurements at different times. For constructing the simplest LG measure K_3 , we therefore map [13, 30]

$$\frac{\Delta t_{21}}{E_0}, \frac{\Delta t_{32}}{E_0}, \frac{\Delta t_{31}}{E_0} \longleftrightarrow \frac{\Delta t_0}{E_{21}}, \frac{\Delta t_0}{E_{32}}, \frac{\Delta t_0}{E_{31}}. \quad (2.6)$$

where $\Delta t_{ij} \equiv t_j - t_i$, and E_{21} , E_{32} , and E_{31} are proxy neutrino energies chosen to satisfy

$$\frac{1}{E_{21}} + \frac{1}{E_{32}} = \frac{1}{E_{31}}. \quad (2.7)$$

In what follows, we refer to each viable combination of such 3 energies as an energy triplet. Eq. (2.7) arises because the three relevant time intervals must also obey the relation

$$\Delta t_{21} + \Delta t_{32} = \Delta t_{31}. \quad (2.8)$$

In the context of LGI violation, the above-described mapping allows us to use available neutrino data at various energies in place of measurements that would otherwise require repeated preparation and measurement at different times. Further, this method depends only on arguments from special relativity and not on the explicit neutrino evolution formula.

2.2 Generalized Leggett-Garg Strings

Eq. (2.2) is one possible definition of the LG measure following the usual time ordering. In general, Leggett–Garg inequalities allow for a broader class of combinations, characterized by arbitrary signs multiplying the correlation functions. More generally, one can define [5, 31, 32]

$$K_n(\{\sigma_i\}) = \sum_{i=1}^n \sigma_i C_{i(i+1)}, \quad (2.9)$$

with the identification $C_{n(n+1)} \equiv C_{n1}$, and where $\sigma_i = \pm 1$. The sign assignments must satisfy the condition

$$\prod_{i=1}^n \sigma_i = -1, \quad (2.10)$$

which ensures that the constructed object is a proper LG string. This generalized approach creates 2^{n-1} independent LGIs for n measurements, each of which, under classical realism, must satisfy

$$|K_n(\{\sigma_i\})| \leq n - 2. \quad (2.11)$$

The standard LG string in eq. (2.2) corresponds to $\sigma_i = 1$ for $i = 1, \dots, n-1$ and $\sigma_n = -1$. However, the freedom of selecting the $\{\sigma_i\}$ allows for optimization: for any given set of measured correlation functions, one may define the optimal LG parameter for a test of classicality as the maximum value over all allowed sign assignments:

$$K_n^{\max} = \max_{\{\sigma_i\}} K_n(\{\sigma_i\}). \quad (2.12)$$

This flexibility can be particularly useful for experimental analyses, as it allows a more robust search for LGI violations by selecting the most sensitive LG string for a given data set [16].

2.2.1 Explicit Leggett-Garg Strings for the Quantum and Classical Cases

For the simplest LG measure K_3 , we can construct four distinct LG strings for both the quantum and classical scenarios. The quantum K_3 strings are given by

$$\begin{aligned} K_3^{Q++} &\equiv C_{12} + C_{23} - C_{31}, \\ K_3^{Q+-} &\equiv C_{12} - C_{23} + C_{31}, \\ K_3^{Q-+} &\equiv -C_{12} + C_{23} + C_{31}, \\ K_3^{Q--} &\equiv -C_{12} - C_{23} - C_{31}. \end{aligned} \quad (2.13)$$

Here, C_{ij} denotes the correlation function between measurements at times t_i and t_j . The superscripts $(++)$, $(+-)$, $(-+)$, and $(--)$ correspond to the sign choices for σ_1 , and σ_2 , with the sign of σ_3 set by $\sigma_1\sigma_2\sigma_3 = -1$.

The corresponding classical expressions for the K_3 strings can be systematically constructed from eq. (2.13) by choosing the appropriate sign assignments. Explicitly, these are

$$\begin{aligned} K_3^{C++} &\equiv C_{12} + C_{23} - C_{12} \cdot C_{23}, \\ K_3^{C+-} &\equiv C_{12} - C_{23} + C_{12} \cdot C_{23}, \\ K_3^{C-+} &\equiv -C_{12} + C_{23} + C_{12} \cdot C_{23}, \\ K_3^{C--} &\equiv -C_{12} - C_{23} - C_{12} \cdot C_{23}, \end{aligned} \quad (2.14)$$

where C_{ij} now denotes the classical correlation function. As in the quantum case, the superscripts indicate the sign choices (σ_1, σ_2) . The recipe outlined above for the classical case closely follows Ref. [13] and will be referred to as the classical Factorized Correlator (FC) method hereafter.

Another way to model the classical case is to fit the correlators in eq. (2.13) with a function $C_{ij} = e^{-\Gamma L/E_{ij}}$ [16] (where E_{ij} corresponds to a particular energy bin), instead of replacing $C_{31} \rightarrow C_{12} C_{23}$. This will be referred to as the classical Exponential Fit (EF) method hereafter.

In practice, in both the quantum and classical cases, one can obtain the string that yields the strongest violation

$$K_3^{\max} = \max \left(K_3^{++}, K_3^{+-}, K_3^{-+}, K_3^{--} \right). \quad (2.15)$$

This enhances the sensitivity of LGI-based tests in experiments. Note that, violation of the LGI in only one of the four LG strings would still be a direct hint for the quantum nature of neutrino oscillations; therefore, the quantity K_3^{\max} allows us to capture the deviation from classicality for such systems in a more efficient manner.

2.2.2 Leggett-Garg Strings in terms of Neutrino Survival Probabilities

In long-baseline neutrino experiments, the effects of all three neutrino flavors need to be considered. However, the system can be reduced to two effective flavors: muon neutrinos, ν_μ , and an effective flavor ν_x representing the combined state of ν_e and ν_τ . We take the dichotomic observable \hat{Q} to give $+1$ for ν_μ and -1 for ν_x . The correlation function C_{ij} is then directly related to the measurable neutrino survival probability $P_{\mu\mu}$ as

$$C_{ij} = 2P_{\mu\mu}(t_i, t_j) - 1. \quad (2.16)$$

Here, $P_{\mu\mu}(t_i, t_j)$ is the probability that a muon neutrino is detected at time t_j , given it was produced as a muon neutrino at time t_i . This allows all LG strings to be expressed solely in terms of neutrino survival probabilities.

Substituting eq. (2.16) into the expressions of eq. (2.13), we obtain the explicit forms for the four K_3 strings in terms of the neutrino survival probabilities

$$\begin{aligned} K_3^{Q++} &= -1 + 2P_{21} + 2P_{32} - 2P_{31}, \\ K_3^{Q+-} &= -1 + 2P_{21} - 2P_{32} + 2P_{31}, \\ K_3^{Q-+} &= -1 - 2P_{21} + 2P_{32} + 2P_{31}, \\ K_3^{Q--} &= 3 - 2P_{21} - 2P_{32} - 2P_{31}, \end{aligned} \quad (2.17)$$

where we define $P_{ij} \equiv P_{\mu\mu}(t_i, t_j)$ for compactness. For the classical FC case, the four K_3 strings can be expressed similarly; eqs. (2.14) and (2.16) together give

$$\begin{aligned} K_3^{C++} &= -3 + 4P_{21} + 4P_{32} - 4P_{21}P_{32}, \\ K_3^{C+-} &= 1 - 4P_{32} + 4P_{21}P_{32}, \\ K_3^{C-+} &= 1 - 4P_{21} + 4P_{21}P_{32}, \\ K_3^{C--} &= 1 - 4P_{21}P_{32}. \end{aligned} \quad (2.18)$$

The replacement $P_{31} \rightarrow P_{21}P_{32} + (1 - P_{21})(1 - P_{32})$ in eq. (2.17) also leads to the set of equations in eq. (2.18).

To estimate the LG strings using the classical Exponential Fit (EF) method (as employed in [16]), we fit the correlator to the form $C_{ij} = e^{-\Gamma L/E_{ij}}$. This does not involve explicit expressions for the LG strings in terms of survival probabilities. Instead, we compute the correlators from $C_{ij} = 2P_{ij} - 1$, taking their associated uncertainties from the muon neutrino survival probability data, and determine the best-fit value of Γ .

By measuring the neutrino survival probability at various energies, one can construct both quantum and classical Leggett-Garg strings directly from experimental data. The comparison of these quantities therefore provides a stringent test of violations of classical macrorealism in the neutrino sector, and allows us to quantify the degree of quantumness in a given neutrino experiment.

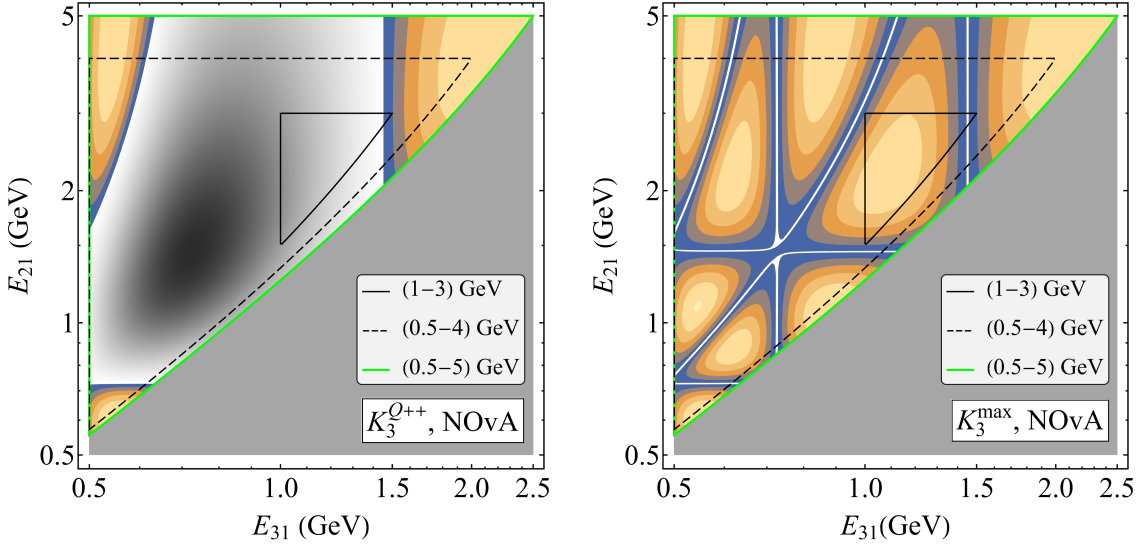


Figure 1. K_3^{Q++} (left panel) and K_3^{\max} (right panel) for the neutrino energies accessible at the NOvA experiment. The axes correspond to neutrino energies E_{31} and E_{21} (see section 2.1), with the shaded region denoting the disallowed values of E_{32} (corresponding to invalid energy triplet choices). The colorful regions denote $K_3 > 1$ values, where the nonclassical behavior of the NOvA experiment may be expected.

2.2.3 Comparing K_3^{Q++} and K_3^{\max}

The LG measure K_3^{Q++} , often used to quantify deviations from classical behavior, provides a standard test of quantumness (e.g., see [13, 26]). However, K_3^{\max} is a more well-suited alternative; it is defined as the maximum over the four LG strings, and therefore captures the largest possible violation of classicality, if there is any.

In fig. 1, we compare these two different quantities for the quantum scenario. We show the quantity K_3^{Q++} in the left panel, and K_3^{\max} in the right panel. The colourful regions denote values of $K_3 > 1$. We use the NOvA experiment for this comparison, and employ benchmark values for the neutrino mixing parameters consistent with the global fit [33–35]:

$$\begin{aligned} \Delta m_{31}^2 &= 2.5 \times 10^{-3} \text{ eV}^2, & \Delta m_{21}^2 &= 7.5 \times 10^{-5} \text{ eV}^2, \\ \theta_{12} &= 33.5^\circ, & \theta_{23} &= 45^\circ, & \theta_{13} &= 8.5^\circ, & \delta_{\text{CP}} &= -90^\circ. \end{aligned} \quad (2.19)$$

The gray triangular region outside the green boundaries is unphysical since, for NOvA, no energy triplet exists in that region. The black and white region in the left panel satisfies the LGI of $K_3 < 1$.

Note that, while the LG measure K_3^{Q++} is able to capture the quantum behavior only for certain regions of the parameter space, the quantity K_3^{\max} captures the violation of the LGI for all available neutrino energies. This demonstrates that considering all possible LG strings through K_3^{\max} can, in principle, significantly increase the likelihood for observation of non-classicality, further motivating the use of this approach in our analyses.

However, in a realistic experiment, the large error bars in the neutrino survival probability can lead to non-trivial complications. Even for the classical case, apparent violations

of the LGI may be observed due to statistical and systematic fluctuations in the values of the neutrino survival probability or the correlation function. Since the relationship $K_3^{\max} \geq K_3^{++}$ always holds, even a purely classical implementation can yield a larger apparent violation of LGI when using K_3^{\max} . In fact, this can, in principle, even lead to an overall reduction in the significance of quantumness for such systems.

Therefore, when using K_3^{\max} , a careful treatment of experimental uncertainties is necessary. A simple way to quantify the degree of quantumness is to count the number of energy triplets that violate the classical bound of $K_3 \leq 1$ in the quantum scenario and compare this with the two classical baselines: the Factorized Correlator (FC) and the Exponential Fit (EF) methods. Furthermore, to enable comparisons across neutrino experiments, one may consider the fraction of energy triplets (quantum and classical) that violate the LGI. This allows for a direct comparison between experiments with different numbers of accessible energy triplet combinations, where for each energy triplet one would obtain a corresponding value of K_3^{\max} .

2.3 The RMS z -score

Although the fraction of triplets that violate the LGI provides a direct qualitative indication that neutrino oscillations are non-classical, it has two important limitations:

1. This quantity is insensitive to the magnitude of violation, i.e., by what amount the LG measure K_3 for a particular triplet exceeds the classical bound. As a result, it carries no information about the statistical significance of the observed violation.
2. In practice, the sparse and non-Gaussian character of the classical distributions is often observed when presenting the fraction of LGI violations. This makes it difficult to quantify the separation between classical and quantum histograms. Hence, it is not straightforward to present a meaningful measure for calculating the significance of classicality violation.

Therefore, in the context of quantumness at neutrino oscillation experiments, Ref. [16] introduced a different metric that assigns weights according to the magnitude of the LGI violations, called the RMS z -score. In section 2.3.2, we will introduce a revised version of the RMS z -score and explain why such a modification is appropriate for LGI tests at neutrino oscillation experiments.

2.3.1 Defining the z -score

First, for each energy triplet, we define four z -scores, corresponding to the four LG strings as

$$\begin{aligned} z^{++} &= \frac{K_3^{++} - 1}{\delta K_3^{++}} , & z^{+-} &= \frac{K_3^{+-} - 1}{\delta K_3^{+-}} , \\ z^{-+} &= \frac{K_3^{-+} - 1}{\delta K_3^{-+}} , & z^{--} &= \frac{K_3^{--} - 1}{\delta K_3^{--}} . \end{aligned} \quad (2.20)$$

Here, the δK_3 denotes the uncertainty in each of the K_3 LG strings, and can be calculated by propagating the error from the experimental survival probability data. In the quantum

case (as well as the classical EF case), each energy triplet (E_{21}, E_{32}, E_{31}) involves three sampled probabilities (P_{21}, P_{32}, P_{31}) . For the quantum scenario, the explicit expressions are

$$\begin{aligned}\delta K_3^{Q++} &= 2\sqrt{(\delta P_{21}^u)^2 + (\delta P_{32}^u)^2 + (\delta P_{31}^l)^2}, \\ \delta K_3^{Q+-} &= 2\sqrt{(\delta P_{21}^u)^2 + (\delta P_{32}^l)^2 + (\delta P_{31}^u)^2}, \\ \delta K_3^{Q-+} &= 2\sqrt{(\delta P_{21}^l)^2 + (\delta P_{32}^u)^2 + (\delta P_{31}^u)^2}, \\ \delta K_3^{Q--} &= 2\sqrt{(\delta P_{21}^l)^2 + (\delta P_{32}^l)^2 + (\delta P_{31}^l)^2}.\end{aligned}\quad (2.21)$$

Here, the notation δP_{ij}^u (δP_{ij}^l) denotes the upper (lower) uncertainty on P_{ij} , allowing for the possibility of asymmetric errors in the measured survival probability. Note that, in the above equations, the error bars correspond to fluctuations in the direction which maximizes the LG strings, and thus allow for a larger value of δK_3^Q strings, i.e., the errors are propagated in the direction that increases the value of the LG string (consistent with obtaining an upper bound on their values). Let us explain this explicitly: the first LG string is given by $K_3^{Q++} = -1 + 2P_{21} + 2P_{32} - 2P_{31}$, therefore, K_3^{Q++} will be larger for larger values of P_{21} and P_{32} , and smaller value of P_{31} , which is why we define δK_3^{Q++} with $(\delta P_{21}^u, \delta P_{32}^u, \delta P_{31}^l)$.

For obtaining the z -scores for the classical EF case, we use the three classical correlators (C_{12}, C_{23}, C_{31}) , with their upper/lower uncertainties propagated similar to the quantum case

$$\begin{aligned}\left[\delta K_3^{C++}\right]_{\text{EF}} &= \sqrt{(\delta C_{12}^u)^2 + (\delta C_{23}^u)^2 + (\delta C_{31}^l)^2}, \\ \left[\delta K_3^{C+-}\right]_{\text{EF}} &= \sqrt{(\delta C_{12}^u)^2 + (\delta C_{23}^l)^2 + (\delta C_{31}^u)^2}, \\ \left[\delta K_3^{C-+}\right]_{\text{EF}} &= \sqrt{(\delta C_{12}^l)^2 + (\delta C_{23}^u)^2 + (\delta C_{31}^u)^2}, \\ \left[\delta K_3^{C--}\right]_{\text{EF}} &= \sqrt{(\delta C_{12}^l)^2 + (\delta C_{23}^l)^2 + (\delta C_{31}^l)^2}.\end{aligned}\quad (2.22)$$

Here, the errors corresponding to the three correlators are propagated from the errors in the survival probability using eq. (2.16); for example, $\delta C_{12}^{u,l} = 2\delta P_{21}^{u,l}$.

Finally, for the classical FC baseline, both the LG strings and their associated uncertainties depend only on P_{21} and P_{32} . Due to the structure of the expressions in eq. (2.18), it is nontrivial to answer whether increasing or decreasing P_{21} or P_{32} values leads to a larger value of the LG strings. To obtain a conservative estimate of the z -scores for the classical FC baseline, i.e., to avoid understating the degree of apparent violation for the classical case, we minimize the denominator of eq. (2.20) by intentionally underestimating

the uncertainties δK_3 . Therefore, we define the errors as

$$\begin{aligned} \left[\delta K_3^{C++} \right]_{\text{FC}} &= 4 \sqrt{(1 - P_{32})^2 (\delta P_{21}^{\min})^2 + (1 - P_{21})^2 (\delta P_{32}^{\min})^2}, \\ \left[\delta K_3^{C+-} \right]_{\text{FC}} &= 4 \sqrt{(P_{32})^2 (\delta P_{21}^{\min})^2 + (P_{21} - 1)^2 (\delta P_{32}^{\min})^2}, \\ \left[\delta K_3^{C-+} \right]_{\text{FC}} &= 4 \sqrt{(P_{32} - 1)^2 (\delta P_{21}^{\min})^2 + (P_{21})^2 (\delta P_{32}^{\min})^2}, \\ \left[\delta K_3^{C--} \right]_{\text{FC}} &= 4 \sqrt{(P_{32})^2 (\delta P_{21}^{\min})^2 + (P_{21})^2 (\delta P_{32}^{\min})^2}. \end{aligned} \quad (2.23)$$

Here, $\delta P_{ij}^{\min} \equiv \min(\delta P_{ij}^u, \delta P_{ij}^l)$ denotes the smaller of the upper and lower uncertainties.

The four z -scores ($z^{++}, z^{+-}, z^{-+}, z^{--}$) allow us to quantify the degree of LG violation for each energy triplet for a given experiment, normalized with respect to the intrinsic uncertainty, for each of the four realizations of the K_3 LG string. We define the final z -score as the maximum between these four quantities and zero,

$$z = \max(z^{++}, z^{+-}, z^{-+}, z^{--}, 0). \quad (2.24)$$

This definition ensures that $z \geq 0$ even in the absence of any LG violation (i.e., the lowest possible value of z -score is zero).

2.3.2 Defining the RMS z -score

We define the aggregate z -RMS statistic as

$$z_{\text{RMS}} = \sqrt{\frac{1}{N} \sum_{i=1}^N z_i^2}, \quad (2.25)$$

with N being the total number of energy triplets. Note that our definition differs from that in Ref. [16]. In Ref. [16], the RMS statistic is normalized by N_{LGV} , which is the number of energy triplets that violate the LGI.

However, normalizing with respect to N_{LGV} can lead to a significant overestimation of the z_{RMS} values, particularly for scenarios with $N_{\text{LGV}} \ll N$, where N is the total number of triplets. For example, let's take 2 experiments with a similar number of total triplets, $\mathcal{O}(N^{(1)}) \approx \mathcal{O}(N^{(2)})$. Further, we take that $\mathcal{O}(N_{\text{LGV}}^{(1)}) \ll \mathcal{O}(N_{\text{LGV}}^{(2)})$. If the z -score values for the LG violating triplets are comparable across the two experiments, then normalizing with N_{LGV} would lead to comparable z_{RMS} values for both experiments. Essentially, this is the opposite problem of simply looking at the fraction of triplets that violate the LGI. In that case, all violations are weighted equally, regardless of their magnitude. In contrast, if one normalizes the RMS z -score by N_{LGV} , the measure becomes insensitive to how many triplets violate the LGI in the first place. However, if we normalize with respect to the total number of triplets N , then the z_{RMS} value for experiment (1), where only a few triplets violate the LGI, would drop significantly. Therefore, in our definition, the z_{RMS} is normalized by N , the total number of triplets, and this allows our measure to accurately represent both the magnitude and frequency of violation of the LGI.

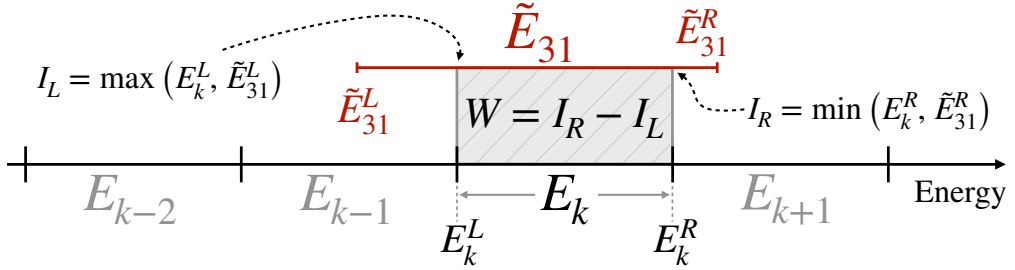


Figure 2. Schematic diagram representing the overlap between the generated energy bin $(\tilde{E}_{31}^L, \tilde{E}_{31}^R)$ and k^{th} experimental energy bin (E_k^L, E_k^R) . The gray shaded area corresponds to the overlapping region where its left and right boundaries are defined by $I_L = \max(E_k^L, \tilde{E}_{31}^L)$ and $I_R = \min(E_k^R, \tilde{E}_{31}^R)$, respectively.

To quantify the degree of deviation from classical behavior, we have to implement a systematic, step-by-step analysis. In what follows, we cover the key details necessary for such an approach.

3 Implementation

In this section, we address some of the key technical challenges, including the effect of asymmetric uncertainties in the neutrino survival probability data and the identification of suitable energy triplets for calculating the LG strings. The framework outlined allows for a direct statistical comparison between quantum and classical scenarios.

3.1 Obtaining the Energy Triplets for the Leggett-Garg Strings

One key step in our study is the systematic determination of energy triplets for testing the LGI. We label the three energies of the triplet as E_{21} , E_{32} , and E_{31} . Each triplet corresponds to three energy ranges (also referred to as bins) which can be specified via their left and right edges, i.e. $E_{ij} \equiv (E_{ij}^L, E_{ij}^R)$. To construct all possible combinations of the energy triplet for an experiment, we first take two of the energy bins directly from experimental data (E_{21} and E_{32}), and then construct the third energy range, E_{31} , such that

$$\tilde{E}_{31}^{L,R} = \left(\frac{1}{E_{21}^{L,R}} + \frac{1}{E_{32}^{L,R}} \right)^{-1} \quad (3.1)$$

is satisfied for both left and right edges. The \tilde{E}_{31} (tilde) denotes that this energy bin is generated from E_{21} and E_{32} .

The resultant $(\tilde{E}_{31}^L, \tilde{E}_{31}^R)$ is typically not going to correlate exactly with any experimental bin, even when E_{21} and E_{32} are obtained directly from the available experimental energy bins. We refer to \tilde{E}_{31} as the “generated” bin in what follows.

Next, we perform a detailed analysis to find the experimental energy bin that maximally overlaps with \tilde{E}_{31} . We first compute the width of the overlap of the generated

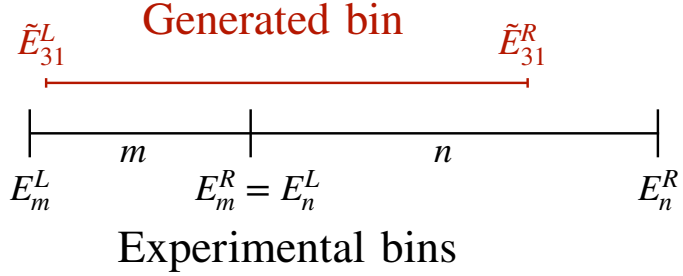


Figure 3. Schematic diagram representing the overlap between the generated energy bin $(\tilde{E}_{31}^L, \tilde{E}_{31}^R)$ and two experimental energy bins (m and n).

interval $(\tilde{E}_{31}^L, \tilde{E}_{31}^R)$ with the k -th experimental bin (E_k^L, E_k^R) , by defining:

$$\begin{aligned} \text{Left edge of the overlap: } & I_L = \max(E_k^L, \tilde{E}_{31}^L) , \\ \text{Right edge of the overlap: } & I_R = \min(E_k^R, \tilde{E}_{31}^R) , \\ \text{Width of overlap: } & W = \max(0, I_R - I_L) . \end{aligned} \quad (3.2)$$

This is shown schematically in fig. 2. For a scenario where the generated energy bin (\tilde{E}_{31}) overlaps with multiple experimental energy bins, we can consider two different ways to measure the amount of relative overlap. In the first method, we divide the width of the overlap (W) by the width of the generated \tilde{E}_{31} energy bin, i.e., we express the overlap relative to the generated energy bin. In the second method, we divide the width of the overlap by the width of the experimental energy bin (E_k) . We express the two definitions as follows:

$$\begin{aligned} O_{\text{gen}} &= \frac{W}{\tilde{E}_{31}^R - \tilde{E}_{31}^L} , \\ O_{\text{exp}} &= \frac{W}{E_k^R - E_k^L} . \end{aligned} \quad (3.3)$$

Here, \tilde{E}_{31}^L and \tilde{E}_{31}^R denote the left and right edges of the generated energy bin, while E_k^L and E_k^R correspond to the left and right edges of the k^{th} experimental energy bin.

The overlap of the generated energy bin with multiple experimental energy bins can lead to non-trivial complications, especially if the width of the experimental energy bins is not uniform. We point out one such scenario in fig. 3 by taking a simple example where one generated energy bin overlaps with two experimental energy bins (denoted as m and n) of unequal width. In the scenario shown in the figure, $O_{\text{gen}}(m) < O_{\text{gen}}(n)$ is satisfied, since energy bin n covers a larger fraction of the $(\tilde{E}_{31}^L, \tilde{E}_{31}^R)$ range. However, a bigger fraction of the energy bin m is covered by the range $(\tilde{E}_{31}^L, \tilde{E}_{31}^R)$ in our example, and thus $O_{\text{exp}}(m) > O_{\text{exp}}(n)$. Therefore, which experimental bin represents best the theoretically generated estimate depends on how we define the overlap. We define the overlap score as the product

$$\text{overlap score} = O_{\text{gen}} \times O_{\text{exp}} , \quad (3.4)$$

so that both arguments are considered in our final selection.

Among all candidate experimental bins considered in the analysis, we select the one with the highest overlap score, identifying it as the best representative of the generated $(\tilde{E}_{31}^L, \tilde{E}_{31}^R)$ interval. For every combination of E_{21} and E_{32} , we first estimate \tilde{E}_{31} in the dataset, and then calculate the overlap score, creating a complete set of viable triplets for each long-baseline neutrino experiment. Our search strategy ensures that for each combination of E_{21} and E_{32} , we find only one suitable E_{31} , i.e., there is no double counting. The procedure devised in this section ensures that the chosen energy triplets are physically well-motivated.

3.2 Sampling in the Presence of Asymmetric Probability Uncertainties

To calculate the LG measures and the RMS z -score, first, we need to assign an oscillation probability (or correlator) value corresponding to an energy bin. To do this, we sample the probability around its mean value and properly deal with the corresponding uncertainty ranges. In many cases, experimental oscillation probability data have asymmetric uncertainties, meaning that the upper and lower error bars have different lengths. To incorporate the effects of these error bars, we introduce a split-Gaussian Monte Carlo (MC) approach to precisely map these uncertainties into our statistical sampling.

We create MC samples for each observable with a measured central value μ with asymmetric uncertainties σ_- (lower) and σ_+ (upper), by following the steps given below:

1. Generate a uniform random variable $u \in [0, 1]$.
2. Compute $w = \sigma_+ / (\sigma_- + \sigma_+)$.
3. If $u < w$, take a sample from the lower Gaussian half

$$x = \mu - |N(0, \sigma_-)| ,$$

otherwise (for $u \geq w$), take a sample from the upper Gaussian half

$$x = \mu + |N(0, \sigma_+)| .$$

Here, $N(0, \sigma)$ denotes a random variate drawn from a normal distribution with mean 0 and standard deviation σ . The absolute value ensures that the fluctuation is oriented away from the center value, and the sign in front ensures that the fluctuation is in the correct direction. In fig. 4, we show the results of the split-Gaussian sampling technique given above, for a mean of $\mu = 0.5$, and $\sigma_+ = 0.1$, $\sigma_- = 0.05$, where we have taken 10^6 MC samples to build the probability density function.

This approach preserves both the central value and the observed asymmetry of the experimental uncertainties. The split-Gaussian sampling is necessary to accurately determine the fraction of triplets that violate LGI, as well as any other observable whose interpretation depends on treating the underlying uncertainties properly.

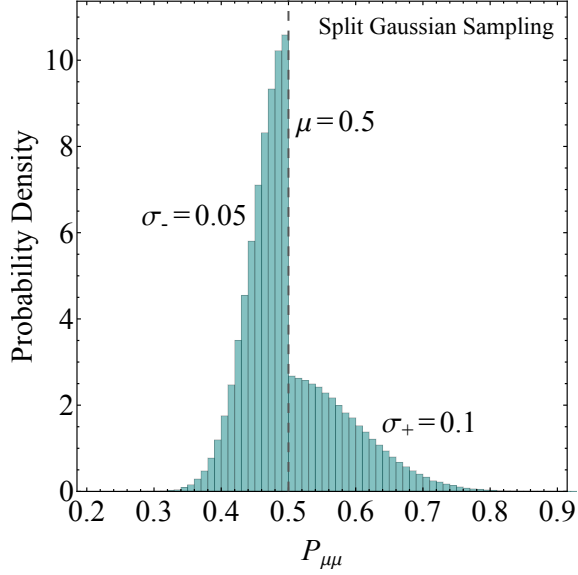


Figure 4. Probability density function obtained through a split-Gaussian sampling of an asymmetric mock oscillation probability distribution, with mean $\mu = 0.5$, and upper and lower standard deviations given by $\sigma_+ = 0.1$, and $\sigma_- = 0.05$, for 10^6 MC samples.

4 Results

In this section, we present the statistical significance of LGI violations for four long-baseline neutrino experiments: MINOS, NOvA, T2K, and DUNE. These neutrino experiments have varying baselines and different neutrino energy ranges, providing complementary probes of the quantum nature of neutrino oscillations. To quantify the quantumness for each experiment, we will be comparing the quantum and classical predictions using (*i*) the distributions of the fraction of energy triplets that violate the LGI and (*ii*) the distributions of the RMS z -score. We construct the relevant distributions by sampling muon neutrino survival probabilities in each energy bin (with mean and standard deviation taken from experimental data), for all energy triplets in a given experiment, and computing both N_{LGV} and z_{RMS} for each sample. This procedure is repeated 10^5 times to obtain accurate representations of the distributions corresponding to quantum and classical behavior.

The quantum scenario follows the procedure outlined in eqs. (2.13) and (2.17). For the classical case, to account for apparent LGI violations that may arise from statistical and systematic uncertainties in the data, we consider two approaches:

1. Classical Factorized Correlator (FC) method: We impose the classical relation $C_{31} = C_{21} \cdot C_{32}$, and express all correlators in terms of survival probabilities, see eq. (2.18) and detailed discussion in section 2. This method was used in [13].
2. Classical Exponential Fit (EF) method: Here, the correlators are modeled as $C_{ij} = \exp(-\Gamma L/E_{ij})$, with the parameter Γ determined from the fit to the data. The uncertainties on C_{ij} are obtained by propagating the experimental errors on the

survival probabilities for each considered experiment. This method was employed in [16].

Before evaluating the significance of LGI violations for each experiment, we briefly summarize the relevant details of the four experiments considered in this work, including the references used for the probability-level data (with associated uncertainties).

MINOS: The Main Injector Neutrino Oscillation Search (MINOS) experiment, located in the US, used a 735 km baseline from Fermilab in Illinois to the Soudan mine in Minnesota. It primarily measured muon-neutrino disappearance with beam energies in the 1–10 GeV range, with the flux peaking at ~ 3 GeV. For the muon neutrino survival probability data used in our analysis, we employ the MINOS results from Ref. [14, 15].

NOvA: The NuMI Off-Axis ν_e Appearance (NOvA) experiment, also in the US, has an 810 km baseline from Fermilab to Ash River, Minnesota. Its off-axis design produces neutrinos mostly between 1 and 4 GeV, with the flux peaked near 2 GeV. In this work, we use the muon neutrino survival probability data from Ref. [36].

T2K: The Tokai to Kamioka (T2K) experiment in Japan sends a neutrino beam from J-PARC in Tokai to the Super-Kamiokande detector in Kamioka, 295 km away. Its off-axis design yields a narrow energy spectrum in the $\sim (0.2\text{--}2)$ GeV energy range, peaked near 0.6 GeV. For T2K, we take the muon neutrino survival probability data from Ref. [37]. This data has not been previously analyzed in the context of quantum behavior at neutrino experiments.

DUNE: The Deep Underground Neutrino Experiment (DUNE), currently under construction in the US, will employ a 1300 km baseline from Fermilab to the Sanford Underground Research Facility (SURF) in South Dakota. This will be the longest baseline for oscillation studies using neutrinos produced in accelerators. DUNE is designed to cover an energy range of $\sim (0.5\text{--}8)$ GeV, with the beam flux peaking around 2.5 GeV. In the absence of any recent and publicly available pseudodata, we construct the mock data as follows.

For DUNE, in the energy range of $(0.5\text{--}7.75)$ GeV, we take bin sizes of 0.25 GeV (leading to 29 energy bins), and for each energy bin, we assign the statistical error in the oscillation probability from Fig. 10 of Ref. [20]. Note that the data in Ref. [20] features a relative error of $1/\sqrt{N_{E_\nu}}$, where N_{E_ν} is the number of events in the energy bin E_ν . Therefore, the statistical error at the probability level can be simply expressed as:

$$\delta P_{\text{stat}}(E_\nu) = P_{\mu\mu}(E_\nu)/\sqrt{N_{E_\nu}} . \quad (4.1)$$

For every energy bin, we compute the oscillation probability by integrating the full three-flavor muon neutrino survival probability over the width of the energy bin and dividing by the bin width. We take a baseline of 1300 km and the oscillation parameters from eq. (2.19). We include systematic errors, taking a benchmark choice of 5% systematic error at the probability level (for the treatment with an array of possible systematic errors, see section 4.5), i.e.,

$$\delta P_{\text{syst}}(E_\nu) = 0.05 . \quad (4.2)$$

Therefore, the total error in each individual energy bin is given by

$$\delta P = \sqrt{(\delta P_{\text{syst}})^2 + (\delta P_{\text{stat}})^2}. \quad (4.3)$$

This simplified treatment of errors differs from a realistic experimental analysis in two aspects: (i) the systematic error is an energy-dependent quantity, and (ii) the error obtained in our analysis is symmetric, with both upper and lower error bars in generated pseudodata being of the same length. Nevertheless, the DUNE results presented in this section hold as a proof-of-concept, and can be updated in the future with actual data. The DUNE results shown in this work correspond to a benchmark with a 5% systematic error, as considered in [38].

4.1 Fraction of Triplets that Violate the Leggett-Garg Inequality

In this section, we compute the fraction of energy triplets that violate the LGI for each of the four considered experiments. The fraction of triplets violating LGI is simply calculated as the ratio of N_{LGV} and N , where N is the total number of triplets. For the quantum scenario, we evaluate the maximum of the four LG strings, K_3^{\max} , as defined in eq. (2.15). We then compare these results against two classical cases, obtained through the FC and EF methods, which quantify the apparent LGI violations arising from statistical and systematic uncertainties.

For each energy bin, we sample the survival probability (or, in the EF method, the corresponding best-fit correlation function), including the effects of the experimental uncertainties, which are often asymmetric: see section 3.2 for a detailed discussion on sampling such asymmetric distributions using the split-Gaussian method. We then form all possible energy triplets and compute the value of K_3^{\max} for the quantum as well as for both classical scenarios (FC and EF). The fraction of triplets satisfying $K_3^{\max} > 1$ is calculated for each scenario.

In the red (quantum), dark cyan (classical FC), and gray (classical EF) histograms shown in fig. 5, we present the resulting fraction of LGI violations for all four experiments considered. We sample the survival probabilities associated with each energy bin, and for every valid energy triplet combination, we compute the corresponding value of K_3^{\max} . This procedure is repeated 10^5 times, yielding the normalized distributions shown in the figure. All four experiments exhibit a very clear deviation from classical expectations, demonstrating the non-classical nature of neutrino oscillations.

Note that, in fig. 5, the histograms representing quantum behavior are approximately Gaussian for MINOS¹, T2K, and DUNE, but skewed to the right for NOvA. For both the classical EF and FC distributions, only MINOS and T2K show Gaussian-like shapes, while NOvA and DUNE data lead to irregular non-Gaussian distributions. For the classical FC method, the sparse nature of the distribution leads to visible gaps in the histograms.

¹Note that, for MINOS, our results do not fully match those from [16], since we use the MINOS data from Ref. [14, 15], while the authors of [16] perform the sampling from the best-fit oscillation model for normal neutrino mass ordering, with the variance of this distribution approximated by the error bars of the MINOS data.

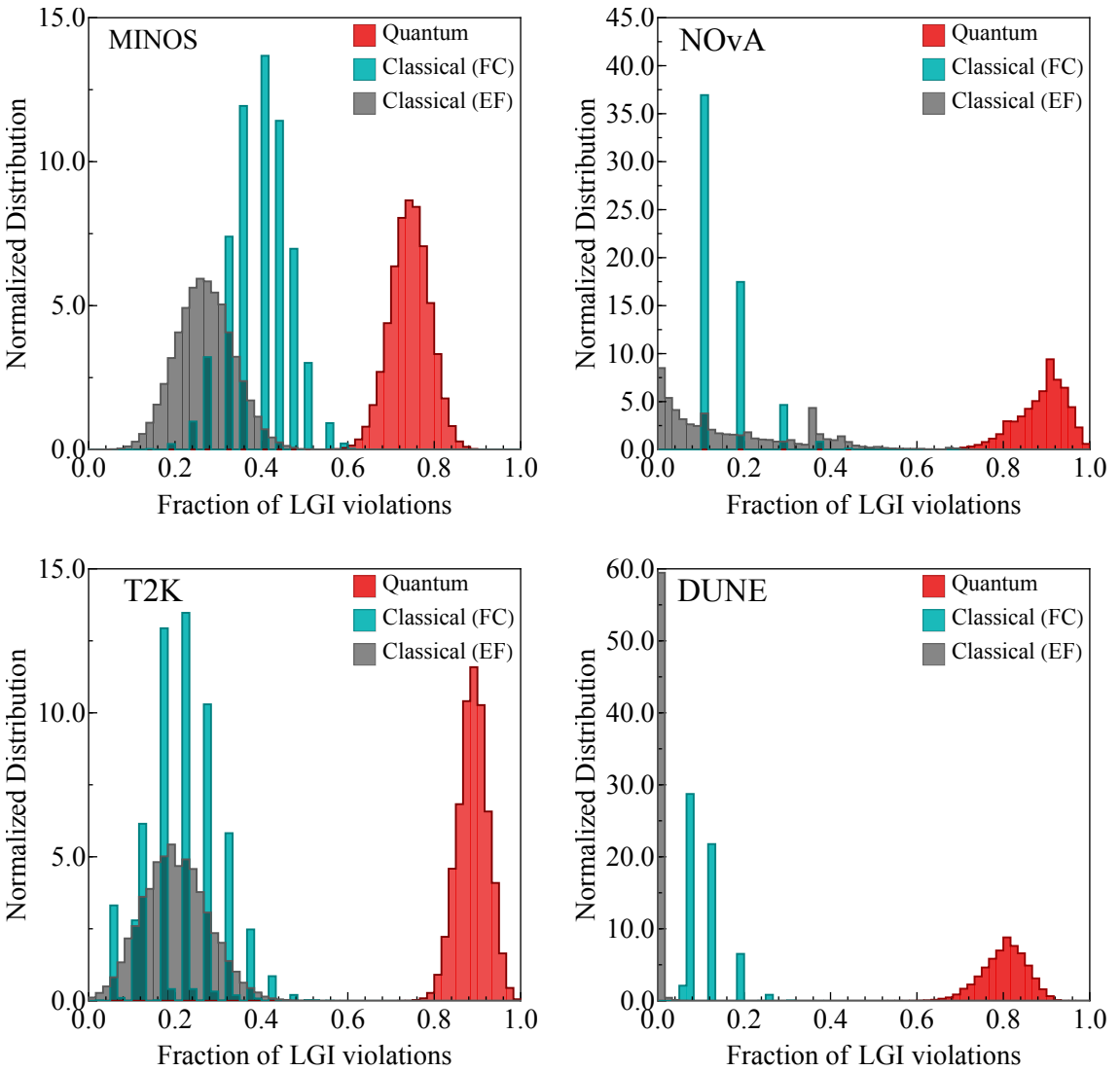


Figure 5. Fraction of energy triplets that violate the Leggett–Garg inequality (LGI) for the four considered long-baseline experiments. The red histograms correspond to the quantum scenario and show that a large fraction of triplets exceeds the classical bound. The cyan histograms represent the classical factorized correlator (FC) method, employed for all 4 LG strings. The gray histograms correspond to the classical exponential fit (EF) method. Comparing the three cases, the quantum distributions clearly exhibit LGI violations, while the classical cases remain concentrated at comparatively smaller values.

These features indicate that although the fraction of triplets violating the LGI, $f_{\text{LGV}} \equiv N_{\text{LGV}}/N$, gives a clear qualitative proof that neutrino oscillations are non-classical, this ratio is not an ideal quantitative measure for our purposes. In particular, even though the distributions corresponding to the quantum scenario are clearly separated from the classical ones, the irregular and sparse character of the classical distributions makes it difficult to quantify the separation between the histograms corresponding to the classical and quantum

scenarios. Further, this measure does not incorporate the degree of LGI violation, as all violations are weighted equally.

Therefore, in what follows, we employ the z -score analysis, which is regulated by both: (i) whether an energy triplet violates the LGI, and (ii) the extent to which it exceeds the classical bound of $K_3 \leq 1$. As we will observe, the distributions of the RMS z -score values provide a robust and quantitative measure of deviation from classicality.

4.2 RMS z -score

To obtain a more quantitative picture of the LGI violations in neutrino experiments, we employ the RMS z -score (z_{RMS}) analysis, described in section 2.3, see in particular eq. (2.25). In fig. 6, we present the z_{RMS} distributions for the four long-baseline experiments: MINOS, NOvA, T2K, and DUNE. Each panel shows the results for the quantum scenario (red) alongside the two classical baselines: FC (cyan) and EF (gray).

In the top left panel of fig. 6, we show the z_{RMS} distributions for the MINOS experiment. Note that, unlike NOvA and T2K, the choice of classical modeling has a strong impact on MINOS: the EF (gray) and FC (cyan) distributions are very clearly separated from each other. We also observe that, among the four experiments, MINOS exhibits the smallest separation between the quantum and classical scenarios (comparing the cyan/gray and red histograms). In fig. 6, our results for MINOS differ from Ref. [16]. This is because:

1. We employ a modified definition of z_{RMS} , normalizing against the total number of energy triplets (N), instead of the number of triplets that violate the LGI (N_{LGV}), see discussions in section 2.3.2;
2. As discussed previously, the authors of Ref. [16] sample the data with the mean defined from the best fit, and the variance taken from the MINOS data, while we sample both the mean and the variance from the data in [14, 15];
3. We remind the reader that we also employ a new method for constructing the viable energy triplets, capturing the realistic experimental energy bin widths, see section 3.1.

We are able to perfectly reproduce the results from Ref. [16] in the absence of the modifications discussed above.

In the top right panel of fig. 6, we show the results for NOvA, where the distance between the classical and quantum distributions is also comparatively small relative to the bottom two panels (T2K and DUNE).

As can be observed in the bottom panels of fig. 6, the z_{RMS} measure is particularly effective at highlighting the non-classical nature of neutrino oscillations in T2K and DUNE. For both experiments, the separation between the quantum and classical distributions is very pronounced.

Further, note that for NOvA, T2K, and DUNE, the classical distributions deviate from a Gaussian shape, primarily due to the RMS nature of the measure, which does not allow the z_{RMS} measure to take a value smaller than zero. Note, however, that the strong sparse nature seen earlier in the f_{LGV} classical FC distributions in fig. 5 is no longer present in the

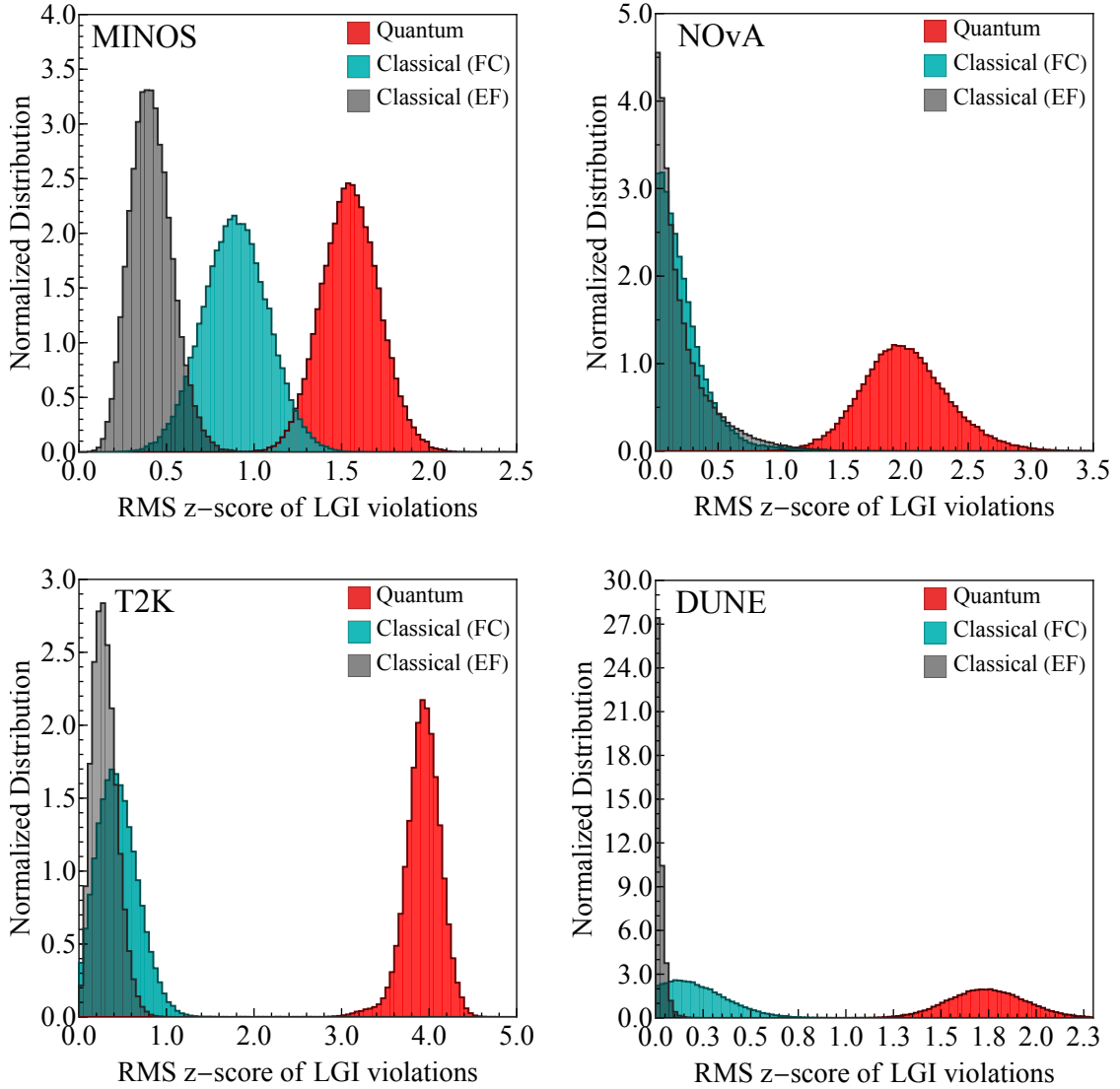


Figure 6. Distributions of the RMS z -score (z_{RMS}) for the four long-baseline experiments: MINOS, NOvA, T2K, and DUNE. The distributions are shown for the quantum (red), classical FC (cyan), and classical EF (gray) scenarios. For NOvA, T2K, and DUNE, the distributions corresponding to quantum scenarios are clearly separated from the classical ones, indicating a significant non-classical behavior.

z_{RMS} analysis. This allows us to fit Gaussian PDFs or CDFs to the resulting quantum and classical distributions and extract best-fit mean values and standard deviations for each scenario.

In what follows, we discuss in detail how the z_{RMS} distributions shown in fig. 6 can be quantified, including the key steps involved in fitting Gaussian PDFs or CDFs, the criteria for choosing between them, and the possible limitations involved.

4.3 Quantifying the Distributions

As shown in fig. 6, all the z_{RMS} distributions for the quantum scenario are approximately Gaussian and can be well described by a standard probability distribution function (PDF) fit. However, the classical baselines (obtained with both the FC and EF method), particularly for NOvA, T2K, and DUNE, remain close to zero and exhibit non-Gaussian shapes. In this section, we describe how to treat the non-Gaussian cases using an effective CDF-based fitting method.

4.3.1 Fitting the Data with Gaussian PDFs

Among the classical EF and FC distributions for the considered long-baseline experiments, only the results for MINOS can be reliably fit with a Gaussian PDF to extract robust best-fit mean values and standard deviations. In contrast, both NOvA and DUNE classical distributions are distinctly non-Gaussian, while the T2K classical distribution is of a partial Gaussian shape.

Nevertheless, even though a fully Gaussian shape is absent, we can still attempt a simple Gaussian PDF fit. Applying such a fit to the NOvA results, we obtain the following best-fit parameters for the two classical cases and for the quantum distribution:

$$\begin{aligned} \mu_{\text{FC}} &= 0.223, \sigma_{\text{FC}} = 0.203, & \mu_{\text{EF}} &= 0.221, \sigma_{\text{EF}} = 0.239, \\ \mu_{\text{Q}} &= 1.996, \sigma_{\text{Q}} = 0.348, \end{aligned} \tag{4.4}$$

with Q denoting the quantum distribution. However, such a PDF-based fit suffers from two important limitations:

1. Robustness of the fit: For non-Gaussian or weakly peaked distributions, the Gaussian fit may not accurately represent the underlying shape. The resulting best-fit parameters can be highly sensitive to fluctuations in the right tail or to minor changes near the peak, leading to unstable or misleading estimates of the mean.
2. Physical interpretation: A naive Gaussian PDF fit may give a negative best-fit mean for the z_{RMS} distribution; this is unphysical given that z_{RMS} is strictly non-negative by construction, see eq. (2.25).

Therefore, we devise an effective CDF-based fitting method, motivated by the observed distribution and more appropriate for our primary aim: quantifying how far the quantum distribution lies from the classical baselines.

4.3.2 Fitting the Data with Gaussian CDFs

To fit the classical distributions using an effective CDF-based approach, we proceed as follows:

1. Using distributions in fig. 6, we compute the empirical CDFs for the classical z_{RMS} values. The empirical CDFs, therefore, give the fraction of samples with z -scores less than or equal to a given value.

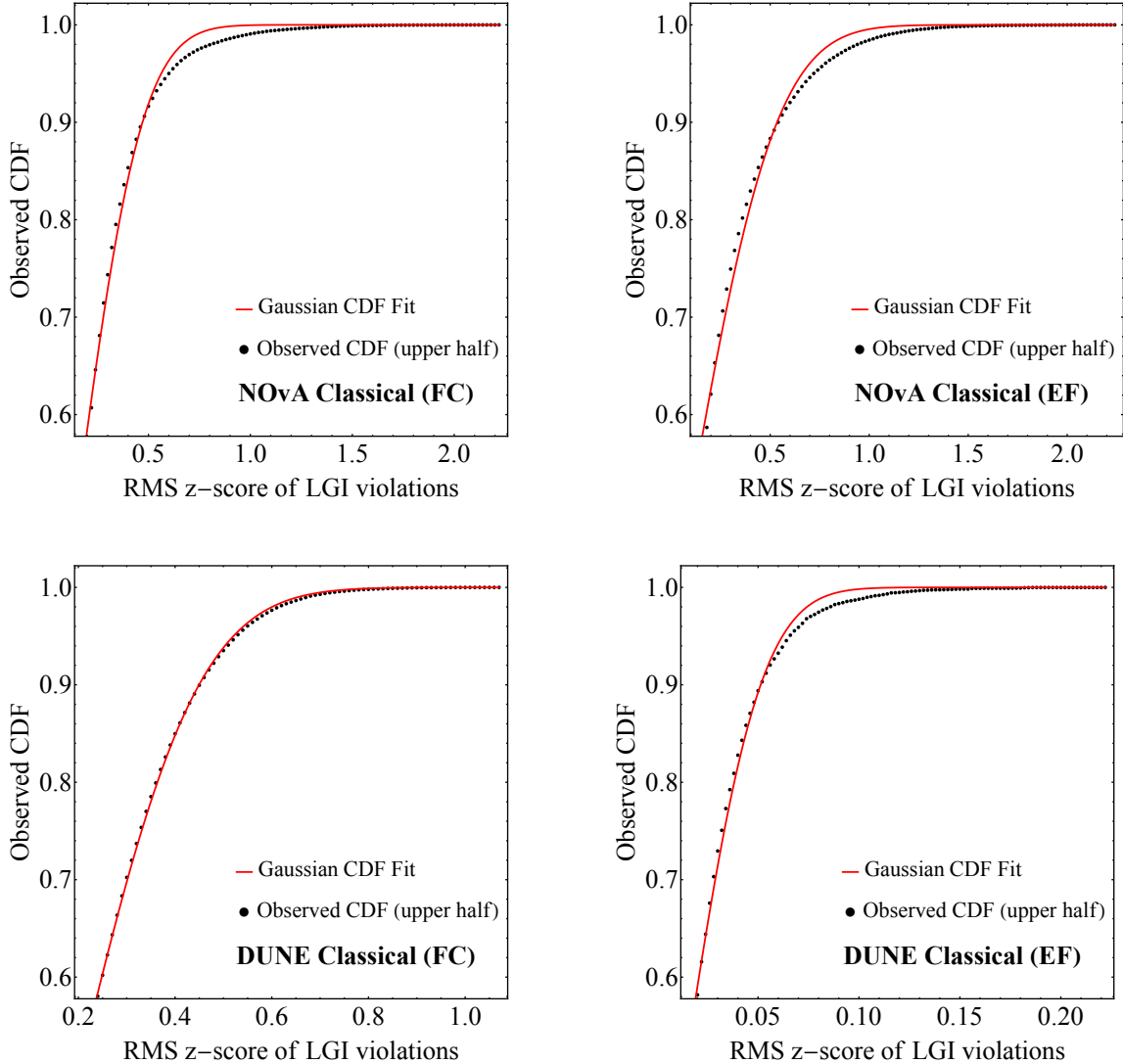


Figure 7. Empirical CDFs (black dotted) for NOvA (top panels) and DUNE (bottom panels) classical z_{RMS} scores, with a best fit (red line) obtained from the upper half of the data using a Gaussian CDF fit method.

2. We focus on the upper half of the data (i.e., z -scores above the median, corresponding to CDF values ≥ 0.5) and fit this portion with a Gaussian CDF, allowing both the mean (μ) and standard deviation (σ) to vary. We observe that the Gaussian CDF best fit yields a smooth and stable representation of the distribution, even when the full shape is non-Gaussian and asymmetric.
3. The resulting best-fit parameters (μ, σ) are extracted separately for the two classical distributions (FC and EF), for each long-baseline experiment.

This method is particularly robust because (i) it relies only on the upper 50% of the data, where the distributions behave more smoothly, and (ii) it captures the physically relevant

Experiment	μ_Q	σ_Q	μ_{FC}	σ_{FC}	μ_{EF}	σ_{EF}
MINOS	1.551	0.164	0.894	0.185	0.414	0.120
NOvA	1.996	0.348	0.146	0.254	0.088	0.348
T2K	3.929	0.204	0.450	0.251	0.298	0.139
DUNE [†]	1.742	0.202	0.198	0.194	0.013	0.029

[†]Uncertainty consisting of statistical error + an uniform 5% systematic error for each energy bin.

Table 1. The mean (μ) and standard deviation (σ) for each of the distributions corresponding to classical (FC and EF) and quantum scenarios, for the four considered long-baseline experiments, obtained through the Gaussian PDF (light brown) and effective CDF (cyan) fit methods.

right tail, whose proximity to the quantum distribution is important for quantifying how closely the classical scenarios can mimic the quantum behavior.

In fig. 7, we show the results of this procedure for the classical (EF and FC) distributions in NOvA (upper panels) and DUNE (lower panels). The black points indicate the empirical CDFs of the classical samples, while the red curves represent the best-fit Gaussian CDFs obtained from fitting the upper 50% of the data. The close agreement between the data and the best fit demonstrates the effectiveness of this method, even when the corresponding histograms are non-Gaussian. For NOvA, the Gaussian CDF fits yield:

$$\mu_{\text{FC}} = 0.146, \sigma_{\text{FC}} = 0.254; \quad \mu_{\text{EF}} = 0.088, \sigma_{\text{EF}} = 0.348. \quad (4.5)$$

These values are in moderate agreement with those obtained from the simple PDF fit (see eq. (4.4)); Note that both the σ_{FC} , and σ_{EF} , obtained through the effective CDF fit, are broader than the values obtained through the PDF fit.

In table 1, we show the best-fit Gaussian parameters (mean and standard deviation) obtained for all 3 histograms (2 classical + 1 quantum) and for the 4 considered experiments. We highlight the DUNE and NOvA classical EF and FC fits with cyan, where the best fits are obtained through the CDF method. The rest are highlighted with light brown, where the Gaussian PDF fit method is employed. With robust best-fit parameters obtained for all quantum and classical distributions, one can quantify how strongly each experiment departs from classicality, i.e., how quantum the behavior of neutrino oscillations is in each experiment.

4.4 Comparing the Significance of Quantumness Across Experiments

We compute the significance of deviations from classical realism for each experiment by using the following formula:

$$N_{\text{Q-Classical}}^{(\sigma)} = \frac{|\mu_Q - \mu_{\text{Classical}}|}{\sigma_{\text{Classical}}}. \quad (4.6)$$

Here, μ_Q is the best-fit mean of the quantum distribution, when fitted with a Gaussian distribution, $\mu_{\text{Classical}}$ and $\sigma_{\text{Classical}}$ are the mean and standard deviation of the Gaussian best fit corresponding to a given classical distribution.

Experiment	$N_{\text{Q-FC}}^{(\sigma)}$	$N_{\text{Q-EF}}^{(\sigma)}$
MINOS	3.55σ	9.48σ
NOvA	7.28σ	5.48σ
T2K	13.86σ	26.12σ
DUNE	7.98σ	58.90σ

Table 2. Statistical significance of quantumness for each of the four considered long-baseline neutrino experiments. The two columns present results for comparison of the quantum distribution against the classical EF and FC cases. The DUNE results correspond to a benchmark with 5% systematic error. For each experiment, we highlight the more conservative result in blue.

In table 2, we show the statistical significance of quantum behavior for each of the four long-baseline neutrino experiments: MINOS, NOvA, T2K, and DUNE. The more conservative result, between the separation of (i) quantum and classical FC predictions, and (ii) quantum and classical EF predictions, is highlighted in blue. Note that comparing against the classical FC method leads to a more conservative statistical significance for MINOS and T2K data, and DUNE benchmark. In contrast, comparing against the classical EF method gives a more conservative answer for NOvA.

The comparatively larger values of $N_{\text{Q-EF}}^{(\sigma)}$ in table 2 arise because the classical EF z_{RMS} distribution has a smaller mean μ_{EF} and a narrower width σ_{EF} . Specifically, the large value of $N_{\text{Q-EF}}^{(\sigma)} \approx 58.9\sigma$ for DUNE can be explained qualitatively through fig. 8, where we show the correlators (C_{ij}) for the best fit obtained via the classical EF method, for MINOS, and DUNE. The smallness of the best fit value $\Gamma = 5.90 \times 10^{-3}$ GeV/km for MINOS allows the classical EF correlator to have values close to 1 (see left panel of fig. 8), especially at lower L/E_{ν} . However, for DUNE we obtain $\Gamma = 1.35 \times 10^{-2}$ GeV/km, which leads to a much smaller correlator. Moreover, the smaller uncertainty on the muon neutrino survival probability for DUNE directly translates into a smaller uncertainty on the correlator C_{ij} . For DUNE, unlike MINOS, the near-zero values of C_{ij} with small uncertainties make the classical EF method less likely to violate the LGI, and even when this happens, the violation is typically small. As a result, the z_{RMS} distribution for DUNE has a small mean and standard deviation, which leads to a large value of $N_{\text{Q-EF}}^{(\sigma)}$.

Among the three existing experiments, we observe the largest significance of quantum behavior at T2K. We would like to stress that following the analysis strategy outlined in [13, 16], we have obtained a comparably large significance for T2K:

$$N_{\text{Q-FC, tol.}}^{(\sigma)} \approx 13.1\sigma, \quad N_{\text{Q-EF, tol.}}^{(\sigma)} \approx 22.9\sigma. \quad (4.7)$$

Given that we found a comparable number of energy triples as in [16] (for a phase tolerance of 5%), $\sim 90\%$ of which coincide across two analyses, the energy triplet selection method clearly does not govern the overall sensitivity. Instead, the large significance stems from the asymmetric uncertainties in the data points, which is characteristic of the analyzed T2K data [37], but not of MINOS data [14, 15]. For T2K, we infer this by considering pseudodata with symmetric uncertainties. Using the upper (lower) error bars in the oscillation probability data as a proxy typically corresponds to larger (smaller) uncertainties.

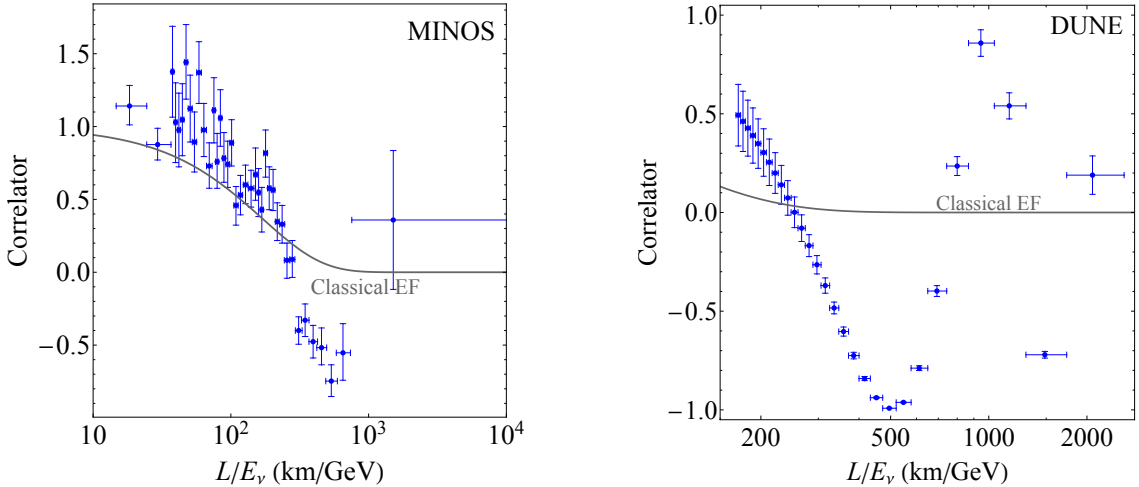


Figure 8. Classical EF best fit for the correlators, for MINOS (left panel) and DUNE (right panel). The gray curve denotes the Classical EF C_{ij} , with the correlator values obtained from the experimental survival probability data shown in blue. For MINOS, the best-fit value is $\Gamma = 5.90 \times 10^{-3}$ GeV/km, and for DUNE, the best-fit curve is obtained for $\Gamma = 1.35 \times 10^{-2}$ GeV/km.

We observe that in the presence of larger (smaller) uncertainties, the mean value of the z_{RMS} quantum distribution is at $\mu_Q \approx 2$ ($\mu_Q \approx 4$). This is because the denominator in the z -score definition is directly affected by the width of the error bars (see section 2.3.1). In fact, for upper (lower) uncertainties in oscillation probability data, we note that the significance of quantumness becomes smaller (larger) than that in eq. (4.7). Therefore, our split-Gaussian sampling method, which can address asymmetric uncertainties in oscillation probability data, is ideal for experiments like T2K. We remind the reader that this work is the first one to analyze the T2K data in the context of quantumness.

4.5 DUNE Results with Varying Systematic Error

We now investigate how the significance of quantumness (defined as the separation between the distributions corresponding to quantum and classical z_{RMS} behaviors) for DUNE changes when a varying systematic uncertainty is included on top of the $1/\sqrt{N_{E_\nu}}$ statistical errors.

For each energy bin (E_ν), the total error is given by $\delta P(E_\nu) = [(\delta P_{\text{syst}})^2 + (\delta P_{\text{stat}})^2]^{1/2}$, where δP_{stat} is the statistical error obtained from eq. (4.1). We remind the reader that in order to obtain the pseudodata, we use the parameters given in eq. (2.19), and follow the same procedure as previously outlined at the beginning of section 4. In our treatment, we take the contribution of the systematic error to be the same for each energy bin.

We vary the systematic error (δP_{syst}) in the range (0.02, 0.1). From the resulting quantum and classical z_{RMS} distributions, we extract their mean values and standard deviations and calculate their separation using eq. (4.6). The results are shown in fig. 9. The separation between the quantum and classical scenarios gradually decreases as the systematic error grows. However, even at the 10% level ($\delta P_{\text{syst}} = 0.1$), the quantum prediction remains several sigma away from both classical constructions, with the classical FC

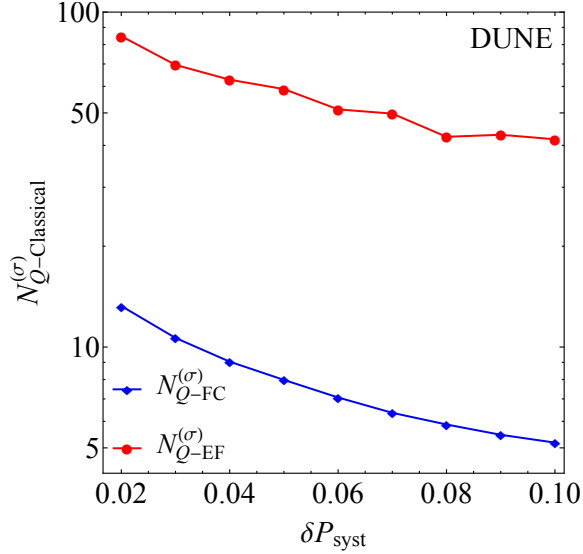


Figure 9. Significance of quantumness at DUNE, compared against the two classical baselines (FC and EF), as a function of the systematic error (δP_{syst}).

baseline consistently producing more conservative results across the whole range of δP_{syst} values. The significance of the classical EF baseline is large due to the extremely narrow classical distribution for the EF scenario. Note that, even for a systematic uncertainty of $\delta P_{\text{syst}} \approx 2\%$, the DUNE significance of quantumness cannot surpass the T2K result.

4.6 Summary of the Results

In summary, the z_{RMS} measure employed makes the separation between the distributions corresponding to quantum and classical scenarios easier to observe and quantify. MINOS, NOvA, T2K, and DUNE all show a significant statistical deviation between the quantum and classical distributions, with T2K giving the strongest result at

$$N_{Q-\text{FC}}^{(\sigma)} \Big|_{\text{T2K}} = 13.86\sigma , \quad (4.8)$$

for the more conservative scenario (quantum vs. classical FC). The main numerical results can be found in tables 1 and 2.

For DUNE, by varying the assumed systematic uncertainty, we find that the significance of quantumness increases with decreasing systematic errors. This behavior is expected and may play an important role in determining the eventual significance of quantum effects observed at DUNE. Overall, our results show that all four long-baseline neutrino experiments exhibit a significant violation of classical realism, and some experiments, like T2K, are clearly more sensitive to the violations of the Leggett–Garg inequality.

5 Conclusions

Neutrino experiments provide an opportunity to study the quantum behavior of nature over hundreds of kilometers of length scales. In this work, we have shown that violations of

classicality can be tested in long-baseline neutrino oscillation experiments. We considered four experiments: MINOS, NOvA, T2K, and DUNE. For each of them, we studied the violations of the Leggett-Garg inequality (LGI) by focusing on the simplest Leggett-Garg (LG) measure K_3 .

We have introduced several improvements that are essential for a reliable analysis of real neutrino data. First, we implemented a fully general treatment of the LG strings by considering all four possible sign assignments (K_3^{++} , K_3^{+-} , K_3^{-+} , and K_3^{--}) and defining K_3^{\max} as the optimal measure, for both the quantum as well as the two classical (Factorized Correlator: FC, and Exponential Fit: EF) scenarios. Second, we constructed energy triplets for each of the neutrino experiments directly from the widths of the energy bins themselves, which allowed us to include the effect of experimental energy bin width in the analysis. Third, we introduced a split-Gaussian sampling scheme to propagate the asymmetric uncertainties present in the muon neutrino survival probability data.

We also showed that the fraction of LGI violations ($f_{\text{LGV}} \equiv N_{\text{LGV}}/N$) measure is generally not statistically well behaved for long-baseline experiments, as the classical distributions are typically sparse and non-Gaussian. To address this, we introduced a modified definition of the z_{RMS} measure, which is sensitive to both the number of energy triplets violating LGI as well as the magnitude of the said violation. Further, for experiments where the classical distributions exhibit non-Gaussian behaviors, we developed an effective CDF-based fitting method by applying a Gaussian CDF fit to the upper half of the empirical distribution.

The combination of (*i*) considering the four sign assignments of the K_3 measure, (*ii*) the modified z_{RMS} definition, (*iii*) energy triplet determination from the experimental data, (*iv*) split-Gaussian sampling of uncertainties, and (*v*) an effective CDF fit procedure provides a general, robust, and reliable framework for determining the degree of quantumness in the neutrino sector. In fig. 6, we presented the z_{RMS} histograms for MINOS, T2K, NOvA, and DUNE, comparing the quantum scenario against the 2 classical cases. We note that all four experiments exhibit a clear and statistically significant departure from classical hypotheses. Taking the most conservative result between the quantum and classical FC as well as quantum and classical EF scenarios, the statistical significance of quantumness for MINOS, NOvA, and T2K reads

$$N_{\text{MINOS}}^{(\sigma)} = 3.55\sigma, \quad N_{\text{NOvA}}^{(\sigma)} = 5.48\sigma, \quad N_{\text{T2K}}^{(\sigma)} = 13.86\sigma, \quad (5.1)$$

and, projection for DUNE (for 5% systematic error) is

$$N_{\text{DUNE}}^{(\sigma)} = 7.98\sigma. \quad (5.2)$$

Note that our T2K result appears to yield the strongest probe of quantumness at neutrino experiments considered to date.

The methods developed in this work apply directly to current datasets and offer a well-defined strategy for future neutrino experiments to probe quantumness. While in this work, we derived the results for the 4 long-baseline neutrino experiments, the pipeline presented is also directly applicable to non-accelerator-based neutrino experiments such as JUNO [39–41], which has recently presented first results.

Acknowledgments

We thank Markus Ahlers, Daniel Cherdack, and Sebastian Shetters for useful correspondence. The work of VB is supported by the United States Department of Energy under Grant No. DESC0025477.

References

- [1] J.S. Bell, *On the Einstein-Podolsky-Rosen paradox*, *Physics Physique Fizika* **1** (1964) 195.
- [2] S.J. Freedman and J.F. Clauser, *Experimental Test of Local Hidden-Variable Theories*, *Phys. Rev. Lett.* **28** (1972) 938.
- [3] A. Aspect, J. Dalibard and G. Roger, *Experimental test of Bell's inequalities using time varying analyzers*, *Phys. Rev. Lett.* **49** (1982) 1804.
- [4] A.J. Leggett and A. Garg, *Quantum mechanics versus macroscopic realism: Is the flux there when nobody looks?*, *Phys. Rev. Lett.* **54** (1985) 857.
- [5] C. Emery, N. Lambert and F. Nori, *Leggett–Garg inequalities*, *Rept. Prog. Phys.* **77** (2013) 016001 [[1304.5133](#)].
- [6] A.J. Leggett, *Testing the limits of quantum mechanics: motivation, state of play, prospects*, *J. Phys. Condens. Matter* **14** (2002) R415.
- [7] J. Kofler and C. Brukner, *Classical world arising out of quantum physics under the restriction of coarse-grained measurements*, *Phys. Rev. Lett.* **99** (2007) 180403 [[quant-ph/0609079](#)].
- [8] T. Fritz, *Quantum correlations in the temporal Clauser–Horne–Shimony–Holt (CHSH) scenario*, *New J. Phys.* **12** (2010) 083055 [[1005.3421](#)].
- [9] J. Kofler and C. Brukner, *The conditions for quantum violation of macroscopic realism*, *Phys. Rev. Lett.* **101** (2008) 090403 [[0706.0668](#)].
- [10] C.D. Tesche, *Can a noninvasive measurement of magnetic flux be performed with superconducting circuits?*, *Phys. Rev. Lett.* **64** (1990) 2358.
- [11] A.J. Leggett and A. Garg, *Comment on “quantum limitations on measurement of magnetic flux”*, *Phys. Rev. Lett.* **63** (1989) 2159.
- [12] M.M. Wilde and A. Mizel, *Addressing the clumsiness loophole in a Leggett–Garg test of macrorealism*, [1001.1777](#).
- [13] J.A. Formaggio, D.I. Kaiser, M.M. Murckyj and T.E. Weiss, *Violation of the Leggett–Garg Inequality in Neutrino Oscillations*, *Phys. Rev. Lett.* **117** (2016) 050402 [[1602.00041](#)].
- [14] MINOS, MINOS+ collaboration, *First MINOS+ Data and New Results from MINOS*, *AIP Conf. Proc.* **1666** (2015) 110004 [[1502.07715](#)].
- [15] MINOS, MINOS+ collaboration, *Results from the MINOS Experiment and New MINOS+ Data*, *PoS NUFAC2014* (2015) 028 [[1507.08564](#)].
- [16] K.M. Groth, J. Ioannou-Nikolaides, D.J. Koskinen and M. Ahlers, *Neutrino Oscillations as a Probe of Macrorealism*, [2504.05375](#).
- [17] T2K collaboration, *The T2K Experiment*, *Nucl. Instrum. Meth. A* **659** (2011) 106 [[1106.1238](#)].

[18] NOvA collaboration, *First Measurement of Neutrino Oscillation Parameters using Neutrinos and Antineutrinos by NOvA*, *Phys. Rev. Lett.* **123** (2019) 151803 [[1906.04907](#)].

[19] DUNE collaboration, *Deep Underground Neutrino Experiment (DUNE), Far Detector Technical Design Report, Volume II: DUNE Physics*, [2002.03005](#).

[20] DUNE collaboration, *Long-baseline neutrino oscillation physics potential of the DUNE experiment*, *Eur. Phys. J. C* **80** (2020) 978 [[2006.16043](#)].

[21] D. Gangopadhyay, D. Home and A.S. Roy, *Probing the Leggett-Garg Inequality for Oscillating Neutral Kaons and Neutrinos*, *Phys. Rev. A* **88** (2013) 022115 [[1304.2761](#)].

[22] D. Gangopadhyay and A.S. Roy, *Three-flavoured neutrino oscillations and the Leggett–Garg inequality*, *Eur. Phys. J. C* **77** (2017) 260 [[1702.04646](#)].

[23] J. Naikoo, A. Kumar Alok, S. Banerjee and S. Uma Sankar, *Leggett-Garg inequality in the context of three flavour neutrino oscillation*, *Phys. Rev. D* **99** (2019) 095001 [[1901.10859](#)].

[24] V.A.S.V. Bittencourt, M. Blasone, S. De Siena and C. Matrella, *Complete complementarity relations for quantum correlations in neutrino oscillations*, *Eur. Phys. J. C* **82** (2022) 566 [[2205.01601](#)].

[25] R.Z. Barrios and M.A. Acero, *Evaluation of the Leggett-Garg inequality by means of the neutrino oscillations observed in reactor and accelerator experiments*, [2401.00240](#).

[26] Q. Fu and X. Chen, *Testing violation of the Leggett–Garg-type inequality in neutrino oscillations of the Daya Bay experiment*, *Eur. Phys. J. C* **77** (2017) 775 [[1705.08601](#)].

[27] X.-Z. Wang and B.-Q. Ma, *New test of neutrino oscillation coherence with Leggett–Garg inequality*, *Eur. Phys. J. C* **82** (2022) 133 [[2201.10597](#)].

[28] DAYA BAY collaboration, *Observation of electron-antineutrino disappearance at Daya Bay*, *Phys. Rev. Lett.* **108** (2012) 171803 [[1203.1669](#)].

[29] KamLAND collaboration, *First results from KamLAND: Evidence for reactor anti-neutrino disappearance*, *Phys. Rev. Lett.* **90** (2003) 021802 [[hep-ex/0212021](#)].

[30] D.S. Chattopadhyay and A. Dighe, *Quantum mismatch: A powerful measure of quantumness in neutrino oscillations*, *Phys. Rev. D* **108** (2023) 112013 [[2304.02475](#)].

[31] J.J. Halliwell, *The Leggett-Garg Inequalities and No-Signalling in Time: A Quasi-Probability Approach*, *Phys. Rev. A* **93** (2016) 022123 [[1508.02271](#)].

[32] M. Blasone, F. Illuminati, L. Petrucciello, K. Simonov and L. Smaldone, *No-signaling-in-time as a condition for macrorealism: the case of neutrino oscillations*, *Eur. Phys. J. C* **83** (2023) 688 [[2211.16931](#)].

[33] P.F. de Salas, D.V. Forero, S. Gariazzo, P. Martínez-Miravé, O. Mena, C.A. Ternes et al., *2020 global reassessment of the neutrino oscillation picture*, *JHEP* **02** (2021) 071 [[2006.11237](#)].

[34] F. Capozzi, E. Di Valentino, E. Lisi, A. Marrone, A. Melchiorri and A. Palazzo, *Unfinished fabric of the three neutrino paradigm*, *Phys. Rev. D* **104** (2021) 083031 [[2107.00532](#)].

[35] I. Esteban, M.C. Gonzalez-Garcia, M. Maltoni, I. Martinez-Soler, J.P. Pinheiro and T. Schwetz, *NuFit-6.0: updated global analysis of three-flavor neutrino oscillations*, *JHEP* **12** (2024) 216 [[2410.05380](#)].

[36] NOvA collaboration, *Recent results from NOvA*, in *56th Rencontres de Moriond on Electroweak Interactions and Unified Theories*, 6, 2022 [[2206.03542](#)].

- [37] P. Dunne, *Latest neutrino oscillation results from t2k*, July, 2020. 10.5281/zenodo.3959558.
- [38] DUNE collaboration, *Long-Baseline Neutrino Facility (LBNF) and Deep Underground Neutrino Experiment (DUNE): Conceptual Design Report, Volume 2: The Physics Program for DUNE at LBNF*, [1512.06148](#).
- [39] JUNO collaboration, *Neutrino Physics with JUNO*, *J. Phys. G* **43** (2016) 030401 [[1507.05613](#)].
- [40] JUNO collaboration, *First measurement of reactor neutrino oscillations at JUNO*, [2511.14593](#).
- [41] JUNO collaboration, *Initial performance results of the JUNO detector*, [2511.14590](#).